Comparison between Topographic and Bathymetric LiDAR Terrain Models in Flood Inundation Estimations

Mahmoud Omer Mahmoud Awadallah *, Ana Juárez and Knut Alfredsen

Department of Civil and Environmental Engineering, Norwegian University of Science and Technology, 7031 Trondheim, Norway; ana.juarez@ntnu.no (A.J.); knut.alfredsen@ntnu.no (K.A.)
* Correspondence: mahmoud.awadallah@ntnu.no

Abstract: Remotely sensed LiDAR data has allowed for more accurate flood map generation through hydraulic simulations. Topographic and bathymetric LiDARs are the two types of LiDAR used, of which the former cannot penetrate water bodies while the latter can. Usually, the topographic LiDAR is more available than bathymetric LiDAR, and it is, therefore, a very interesting data source for flood mapping. In this study, we made comparisons between flood inundation maps from several flood scenarios generated by the HEC-RAS 2D model for 11 sites in Norway using both bathymetric and topographic terrain models. The main objective is to investigate the accuracy of the flood inundations generated from the plain topographic LiDAR, the links of the inaccuracies with geomorphic features, and the potential of using corrections for missing underwater geometry in the topographic LiDAR data to improve accuracy. The results show that the difference in inundation between topographic and bathymetric LiDAR models decreases with increasing the flood size, and this trend was found to be correlated with the amount of protection embankments in the reach. In reaches where considerable embankments are constructed, the difference between the inundations increases until the embankments are overtopped and then returns to the general trend. In addition, the magnitude of the inundation error was found to correlate positively with the sinuosity and embankment coverage and negatively with the angle of the bank. Corrections were conducted by modifying the flood discharge based on the flight discharge of the topographic LiDAR or by correcting the topographic LiDAR terrain based on the volume of the flight discharge, where the latter method generally gave better improvements.

Keywords: LiDAR; topographic; bathymetric; flood inundation; HEC-RAS; hydraulic modeling

1. Introduction

Floods are one of the most adverse natural disasters that threaten human settlements and activities. In Europe, river floods are the most common natural catastrophe, resulting in significant economic loss through direct damages to properties, infrastructures, and agricultural lands and through indirect losses within the affected areas [1]. Moreover, the situation is projected to worsen as recent scenarios of global warming are expected to increase the frequency and the intensity of extreme precipitation events in addition to flood levels [2–5].

Floods can be categorized into two forms: pluvial floods, which are generated mainly by excess rainfall, and topography, where the exceedance of the infiltration capacity creates inundation [6–8], and fluvial floods, where an overflowing water body rises and inundates the adjacent floodplains. The causes of this rise can be a result of excess rainfall in the upstream part, snowmelt, landslides in the lake or reservoir, or river blockages [9]. The simulation of fluvial floods is maintained by hydraulic simulations at which the terrain model, or the digital elevation model, is one of the backbone inputs.

The U.S. Geological Survey (USGS) [10] defined digital elevation models (DEMs) as regularly spaced arrays of elevation values that are referenced horizontally to a specific geographic or projected coordinate system. DEMs can be generated from many sources such as

ground-based surveys, digitizing hard copies of existing topographic maps, or by utilizing remote sensing. Remotely sensed DEMs have been the most used type of terrain models for flood studies recently, and the Shuttle Radar Topography Mission (SRTM) is the most used DEM type, thanks to its availability, acceptable resolution, and accuracy [11]. Accurate DEMs have vital importance in supporting the modeling of environmental processes [12], and especially for flood simulation, they have contributed positively to flood studies due to their detailed topographic information [13,14]. The availability of the SRTM DEMs even in sparse data regions has contributed to its widespread use for flood modeling. However, the inability of SRTM to represent complex city's landscapes with coarse resolution (30 m or 90 m), in addition to the failure of the originator radar to penetrate vegetation, hinders its ultimate use in flood applications [11]. Therefore, advancement in remote sensing technology was required to tackle the SRTM deficiencies, and one of the most interesting emerging technology is Light Detection And Ranging (LiDAR).

LiDAR is a remote sensing technology that enables rapid and accurate development of actual 3-dimensional terrain models. The technology measures the distance to a target by detecting the time between the emission of a pulse of laser light from a sensor and the time of detection of light reflected from the target [15]. The generated DEMs from LiDAR has many advantages over other remote sensing technologies. For instance, LiDAR data could be acquired in the day, at night, and even during cloudy conditions [16,17]. It can penetrate vegetative areas and go in between urban structures more easily, and it can reach centimeters of DEM's accuracy. The studies of Bhuyian and Kalyanapu [18], McClean et al. [19], and Muthusamy et al. [20] compared the flood inundations generated by LiDAR DEMs against other remote sensed DEMs. They found that the flood extent generated by LiDAR produced the closest inundations to reality, while the other remote sensing DEMs were associated with larger overestimation of the inundations. This was found to be linked with the horizontal resolution where the finer the resolution results in more accurate inundations and provide more clearer definition of the river channel.

However, even with the powerful horizontal resolution capabilities of the LiDAR, topographic LiDAR is responsible for generating erroneous inundations attributed to its misrepresentation of the river bathymetry. The topographic (Red) LiDAR (*RL*) is obtained by infrared laser of a wavelength that is unable to penetrate the water and, hence, captures the underwater [21]. Many studies have inspected this type of error by implementing measured field bathymetry to the *RL* DEM [22–25] and concluded that omitting the bathymetric data will result in an overestimation of the simulated inundations. However, recent advances in LiDAR technology have led to the development of bathymetric (Green) LiDAR (*GL*), which, unlike the *RL*, can penetrate the water since it uses blue/green laser beams [26–29]. However, no studies have conducted an explicit comparison between *GL* and *RL* DEMs regarding flood estimation. Presently, 80% of Norway is covered with the *RL*, and full coverage is expected by 2023 [30]. *GL*, on the other hand, is still only available for a few rivers. Since the *RL* currently is far more available than the *GL*, it has been used for simulating large floods with the assumption that the sub-surface storage is less important when the total discharge is very high. It is, therefore, useful to compare a pure *RL* DEM and a combined *RL* and *GL* DEM in terms of estimating flood inundations. Moreover, in all the studies that have addressed the error associated with the missing or inadequate bathymetry, no study has linked the error in inundation to the geomorphic features of the river, which could be a method to pre-determine the potential errors in a project. This paper seeks to answer the following research questions by comparing DEMs made by both bathymetric and topographic LiDAR:

Can we use the topographic LiDAR DEM directly for flood studies? How does the inundation error vary with different flood sizes?

What is the relationship between the inundation error and the geomorphic features of the rivers' channel? Can those features be employed to estimate if topographic DEMs can be used and the potential errors this will lead to?

Can the correction methods that are suggested in the literature help to reduce the inundation error when the topographic LiDAR is used? To what extent can it improve having the various rivers' features?

2. Data

2.1. Study Sites

A total of 11 sites in Norway were selected in this study based on the availability of both bathymetric and topographic LiDAR data in each reach. The sites are in five counties (three sites in Trøndelag, four sites in Møre og Romsdal, two sites in Vestland, and one site each in Viken and Vestfold og Telemark). All the reaches drain mountainous areas and pass-through rural landscapes. The locations of the sites are shown in Figure 1, together with information on reaches' length and the flood regime.

	Sites	Reach Length (km)	Flood regime
1	Driva	11.63	Spring
2	Eidselva	8.91	Autumn
3	Gaula	26.44	Spring
4	Lower Lærdal	14.60	Spring
5	Lower Surna	18.98	Autumn
6	Storåne	4.39	Spring
7	Tokke	4.20	Autumn
8	Upper Lærdal	8.33	Spring
9	Upper Surna	10.91	Autumn
10	Sokna	3.35	Spring
11	Gaua	1.42	Spring
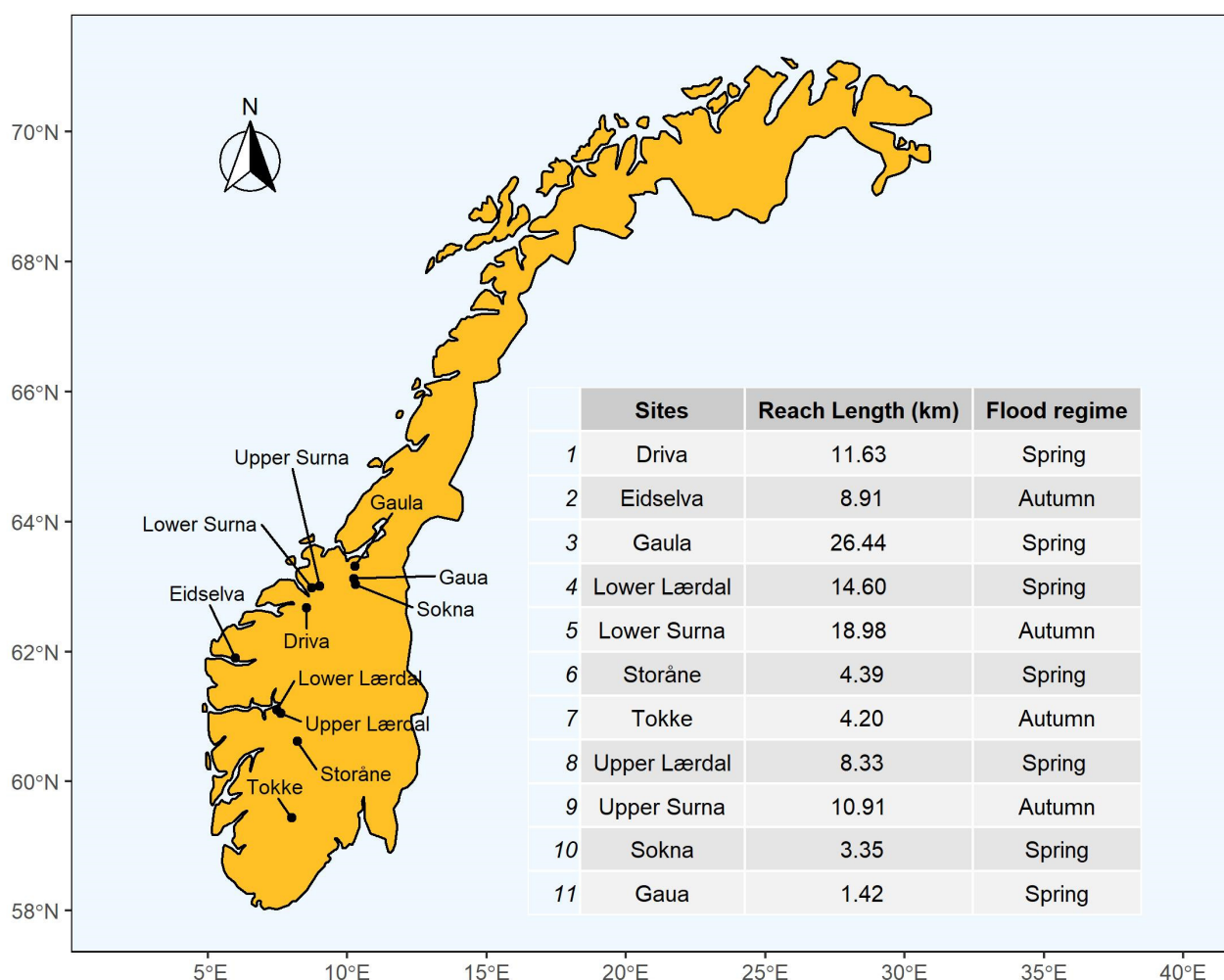
Figure 1. The location of the reaches in Norway, their lengths calculated from NVE's geodatabase, and flood regimes as reported by Gottschalk et al. [31]. Spring flood is predominantly a snowmelt flood, while the autumn flood is mainly driven by rainfall.

2.2. LiDAR Data

General descriptions for the tested sites and their LiDAR data are shown in Table 1. The sites cover a wide range of river sizes from Gaula reach having the largest catchment area of 3086 km^2 to Gaua, a tributary to Gaula, with the smallest catchment area of 85 km^2. All the sites have good quality LiDAR data with a maximum horizontal resolution of 0.5 m and 0.25 m in most of the sites. The topographic LiDAR DEM was generated by the Norwegian

Mapping Authority and made available through the website www.xn--hydedata-54a.no (accessed on 15 February 2021).

Table 1. General descriptions of the sites' sizes and the LiDAR data properties.

Site	Catchment Area (km²)	Mean Discharge (m³/s)	*RL* Resolution (m)	*RL* Point Density (Points/m²)	*RL* Flow (m³/s)	*GL* Resolution (m)	*GL* Point Density (Points/m²)	*GL* Laser Scanner
Driva	2436	63.6	0.5	2	74	0.25	4	Optech Titan
Eidselva	386	23.4	0.25	5	17.6	0.25	4	Optech Titan
Gaula	3086	83.3	0.25	6	146	0.25	5	Optech Titan
Lower Lærdal	994	30.7	0.5	2	14	0.25	5	VQ880-G (RIEGL)
Lower Surna	910	40.6	0.5	2	20	0.5	NA	VQ880-G (RIEGL)
Storåne [1]	770	24.5	0.25	5	6.8 / 35.9	0.2	20	VQ880-G (RIEGL)
Tokke	2332	89.5	0.25	5	22.9	0.25	20	VQ880-G (RIEGL)
Upper Lærdal [2]	750	23.0	0.25 / 0.5	5 / 2	26 / 13	0.25 / 0.25	5 / 5	VQ880-G (RIEGL)
Upper Surna	445	17.4	0.5	2	NA	0.5	NA	VQ880-G (RIEGL)
Sokna	564	13.0	0.25	5	15	0.25	5	Optech Titan
Gaua	84.6	2.0	0.25	6	1.5	0.25	5	Optech Titan

[1] has two LiDAR flow values because of the powerplant outlet in the mid of the reach. [2] has two different *RL* DEMs cover the reach. *RL* and *GL* denotes Red LiDAR and Green LiDAR, respectively.

2.3. Flood Data

The flood discharges for the sites used in the simulation are shown in Table 2. For eight sites, the simulated discharges were found in flood reports published by the Norwegian Water Resources and Energy Directorate (NVE). The discharges for the rest were taken from the NVE website, www.nevina.no (accessed on 15 February 2021), which provides unregulated flood discharges for the Norwegian rivers based on a regional flood frequency analysis [32].

Table 2. Flood scenarios discharges for the sites (in m³/s).

Site	Q M	Q 10	Q 20	Q 50	Q 100	Q 200	Q 500
Driva	545	725	795	885	960	1025	1115
Eidselva	66	86	93	101	107	112	118
Gaula	1041	1551	1800	2144	2404	2685	3070
Lower Lærdal	235	380	470	570	700	800	890
Lower Surna	229	342	391	454	501	549	613
Storåne *	196	290	327	374	410	446	493
Tokke	204	289	323	366	406	443	492
Upper Lærdal	215	310	350	398	452	495	538
Upper Surna	171	230	254	284	306	328	355
Sokna *	125	194	221	257	284	311	347
Gaua *	21.9	34.5	39.5	46.1	51.1	56.2	63.1

* Unregulated flood scenarios retrieved from www.nevina.no (accessed on 15 February 2021).

3. Methodology

To study the differences in inundations between the different LiDAR data, a methodology of many steps was followed and summarized in the flow diagram in Figure A1 in Appendix A.

3.1. DEM Generation for the LiDAR Models

Two different terrain models for each site were constructed using the LiDAR data. The *RL* terrain model was constructed using topographic LiDAR data covering the main channel and the floodplains. The *GL* data, on the other hand, are limited to the river bathymetry in most cases. Therefore, the *GL* terrain models were constructed by merging the *GL* data of the main river channel and the *RL* data of the floodplains. Figure 2 shows an example of the two terrain models for the Driva site.
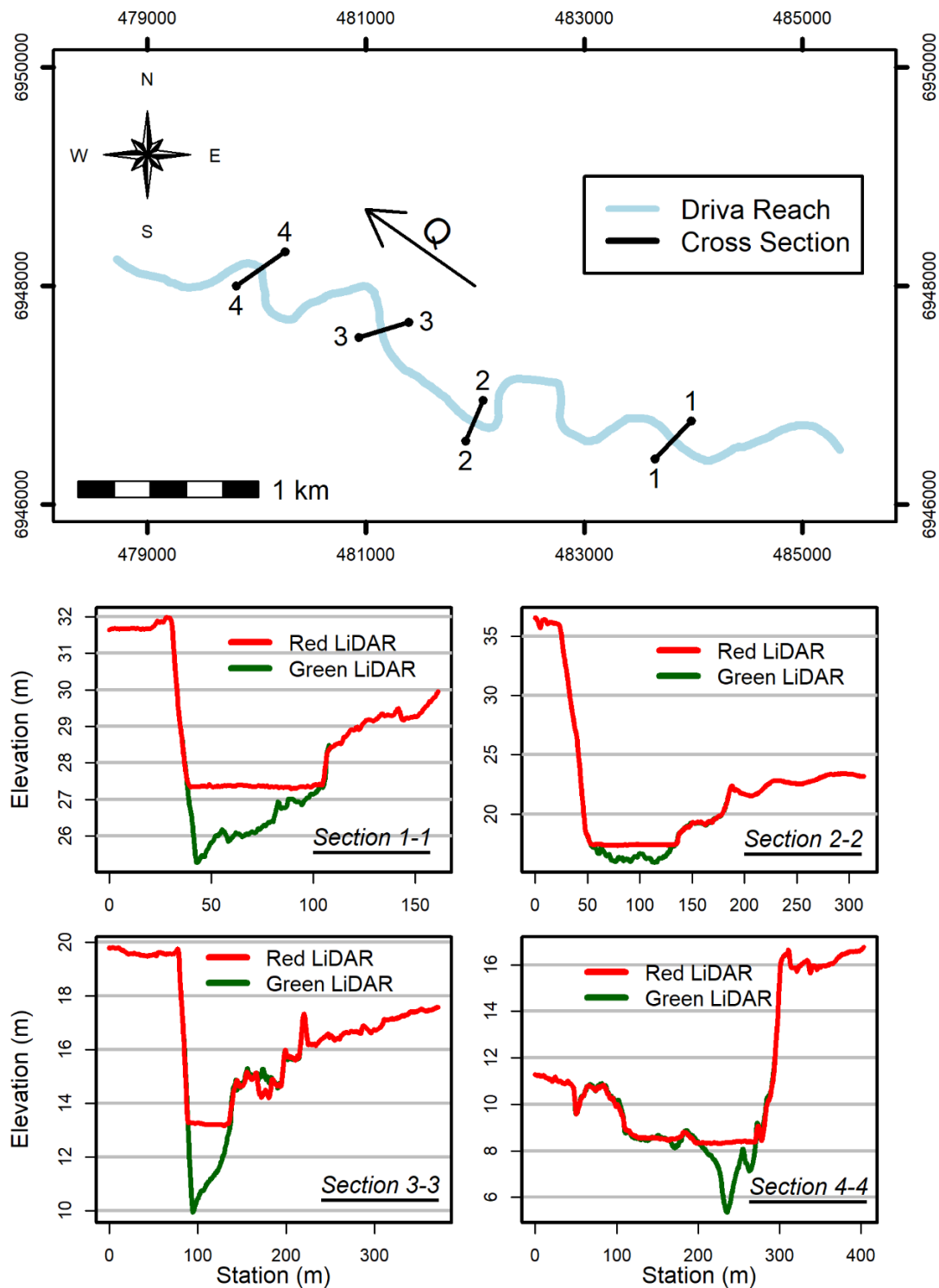
Figure 2. Visual comparison of the LiDAR terrain models for Driva site.

3.2. Hydraulic Simulation

The Hydrologic Engineering Center's River Analysis System two-dimensional hydraulic software (HEC-RAS 6.0) was employed to simulate the flood inundations for the sites. The software has been developed by the US Army Corps of Engineers [33], and has been utilized in many studies focusing upon the influence of the topographic inputs on the flood inundation models [22,25,34]. The simplified Saint-Venant equation, the diffusive wave, was used as the flow representation [35].

To ensure a common base of comparison, the two models of each site differed only in the terrain models while the rest of the model setups were identical. A computational mesh of 5 m was used for all the sites. The Manning's coefficients were assigned according to the literature, 0.03 and 0.06 s/m$^{1/3}$ for the mainstream and the floodplains, respectively [36]. A constant flow hydrograph of the flood discharge as an upstream boundary condition and the normal depth as a downstream boundary condition was used. It is important to mention that this study aims to check the variation in flood inundations resulting from using the various LiDAR terrains. Therefore, the results cannot be taken as referenced flood inundations directly for the sites.

3.3. Terrain Analysis

One of the objectives of the study is to investigate the link between the difference in inundation and geomorphic parameters of the river. The investigated parameters are described below.

3.3.1. Longitudinal Slope, Sinuosity, and Flood Wall Coverage of the Reach

The longitudinal slope of the river is one of the key parameters that define the flow in the open channel flow systems [36], and therefore it has been considered in the investigations as one of the parameters that could define how the inundation error progresses. For each reach, the parameter was estimated by the ratio between the elevation difference of the starting and ending points and the reach length. The sinuosity was also taken into consideration and has been estimated by the ratio of the actual meandered length of the reach and the straight line connecting the starting and ending points of the reach. The coverage of the reach with flood protection embankments will to a great extent, affect the inundation of the reach. Embankment coverage was computed based on data provided by NVE on the website www.nedlasting.nve.no/gis (accessed on 15 April 2021). The percentage of the embankment coverage was computed by the ratio between the length of the embankment on the reach and twice the reach's length to consider the floodplain on both sides of the river.

3.3.2. Missed LiDAR Volume

The subsurface volume left uncaptured by the *RL* measurement for each reach was estimated using the Raster Calculator and Zonal Statistic tools in ArcGIS. The total volume was summed and divided by the length of the reach to make it comparable between rivers.

3.3.3. Bank Slope

The shape of the riverbank is a factor that is expected to explain the difference in inundation between *RL* and *GL* models. Unlike the previous parameters, this parameter was computed at a cross-sectional level along the reach and extracted by automating a series of tools in ArcGIS Pro. To capture the shape variability of the slope, 10 layers were created in the confined region between the bottom of the river and the maximum water level resulting from the 500-years scenario. The side slopes between each layer were found by calculating the horizontal distance (*Z*) of the sloped surface with respect to a unit elevation difference. The normal distance between the river centerline and the bank is the horizontal length (*L*). *Z* is calculated by the ratio between the difference in the horizontal

distances where the successive layers meet the bank and the difference in the elevations of the two layers (*M*). *Z* could be calculated by the following equation:

$$Z = \frac{L_{i+1} - L_i}{M_{i+1} - M_i} \tag{1}$$

where (*i*) and (*i* + 1) are the lower and the upper layers, respectively. The bank's slopes between the 10 layers were found for the left and the right sides of the reach. The selection of which bank slopes to include in a cross-section for each flood scenario was based on the Water Surface Elevation (WSE) of that scenario and the WSE at the mean-flood of the *GL* model. The first layer that has an elevation immediately below the WSE of the *GL* at the mean-flood scenario was specified as the lowest layer, and the layer that has an elevation right higher than the 500-years scenario on the *RL* was set as the highest layer. From the selected layers, the mean and the standard deviation of the bank slope were computed. The horizontal distance of the slope (*Z*) was finally converted into degrees.

3.4. Evaluation of the Flood Extents

The evaluation of the variations in inundation was carried out on both reach and transect scales. For the reach scale, the error was computed based on the total inundation area of a certain flood scenario. Then the *Normalized Error* was implemented as a measurement to quantify the overestimation in inundation from the *GL* DEM that was created by *RL* DEM and was calculated as follows:

$$Normalized\ Error = \frac{RL\ Inundation}{GL\ Inundation} \tag{2}$$

where *RL Inundation* is the flood extent for a flood scenario produced by the *RL* model and *GL Inundation* is the flood extent for the same flood scenario produced by the *GL* model. Therefore, the closer this parameter to 1, the closer the resulting inundation to the actual flood extent, which is assumed here to be the *GL Inundation*.

For the transect scale, the percentage of deviation of the *RL Inundation* from the *GL Inundation* was calculated on the *Inundation Error* as follows:

$$Inundation\ Error\ (\%) = \frac{RL\ Inundation\ Length - GL\ Inundation\ Length}{GL\ Inundation\ Length} \times 100 \tag{3}$$

where *RL Inundation Length* is the length of the inundated transect on the *RL* model (m) and *GL Inundation Length* is the length of the inundated transect on the *GL* model (m).

3.5. Statistical Tests

A correlation test was performed to investigate the levels of the inundation error for the different site and its relationship with the extracted terrain parameters. The expectation of the inundation error (mean) from all the scenarios was set as a representative for the level the inundation error for each site. The correlation test was conducted using the R Corrplot package [37]. The Pearson correlation coefficient (r^2) was computed, and parameters were evaluated using a significance level of $\alpha < 0.05$.

To test the dependency of the inundation error's shape on the embankment coverage percentage, a one-way analysis of variance (ANOVA) test was conducted. The test was conducted using Anova function of the Car package in R [38]. The shapes of the inundation were coded as 0 and 1, and the significance of the embankment percentage was evaluated by F-statistics corresponding to a significance level of $\alpha < 0.05$. Based on the analysis, the amount of the embankment percentage that corresponds to the change in the error shape was estimated.

3.6. Correction Methods

Some corrections of flood inundation models were proposed [22,35] in situations where no bathymetry data were available. The two correction techniques for the *RL* flood models tested in this study were the Discharge Correction Technique (DCT) and the Terrain Correction Technique (TCT). DCT is a correction technique that is based on correcting the discharge of the flood scenario and compensates the missing river bathymetry by subtracting the discharge at the *RL* acquisition from the flood discharge. TCT, on the other hand, is a correction on the *RL* terrain model itself in which it carves out the flow area from the terrain model before using it for simulations. This correction was applied by burning the depth layer resulting from simulating the *RL* acquisition discharge in the HEC-RAS 2D model into the *RL* DEM. The performance of the proposed corrections was evaluated by computing the reduction in the *RL* error that resulted from applying the correction as follows:

$$Error\ Reduction\ (\%) = \left(\frac{RL\ Inundation - Correction\ Inundation}{RL\ Inundation - GL\ Inundation} \right) \times 100 \qquad (4)$$

where *Correction Inundation* is the inundated area resulted from either DCT or TCT for each flood scenario. These corrections were tested on Guala and Lower Lærdal reaches.

4. Results

4.1. Terrain Analysis Outputs

Table 3 shows a summary of the terrain analysis parameters that were extracted from the two DEMs of the LiDAR. Gaula had the largest missed LiDAR volume with 141 m^3 subsurface volume missed per meter length, while Storåne showed the lowest missed volume with 4 m^3 per meter length. Gaula had the mildest longitudinal slope with 0.12%, while the highest slope was found in Upper Lærdal with 1.9%. For the sinuosity, Eidselva showed the highest sinuosity with 1.83, while Gaua and Upper Surna showed the lowest among the reaches with 1.14. Lower Lærdal and Gaula showed to be the most flood-protected reaches with coverages of 72 and 62%, respectively, while Storåne and Upper Lærdal showed the least protection with 0 and 3% coverages, respectively.

Table 3. Terrain analysis outputs for the 11 sites.

Site	Missed LiDAR Volume (m³/m)	Slope (%)	Sinuosity	Flood Protection Coverage (%)	Mean Bank's Slope (Degrees)
Driva	17	0.29	1.37	24	2.97
Eidselva	26	0.49	1.84	11	9.88
Gaula	141	0.12	1.33	62	1.66
Lower Lærdal	8	0.42	1.63	72	2.15
Lower Surna	36	0.14	1.27	25	2.41
Storåne	4	0.57	1.25	0	3.25
Tokke	27	0.51	1.29	15	11.24
Upper Lærdal	5	1.90	1.35	3	19.54
Upper Surna	5	0.36	1.14	20	5.82
Sokna	15	0.92	1.15	39	15.01
Gaua	5	0.46	1.14	15	4.76

Figure 3a shows the longitudinal profiles for the sites. Upper Lærdal showed to be the steepest site, while Lower Surna and Gaula were the sites with the mildest running slope.

Figure 3b shows density plots of the variations of the bank slope for each site. Lower Lærdal showed the largest proportions of the reach with bank slopes less than 3 degrees, followed by Gaula and Lower Surna. Storåne, Driva, and Gaua have their peaks densities at

values less than 3 degrees but at least one-third of the slopes greater. Upper Lærdal, Sokna, and Tokke, on the other hand, appeared as the largest percentage of bank slopes greater than 10 degrees. Two sites fell outside the above categories, Eidselva and Upper Surna, which both showed almost symmetrical bank slope distributions. Upper Surna appeared with a narrow peak distribution while Eidselva showed broad peak ranges between 3 and 30 degrees.
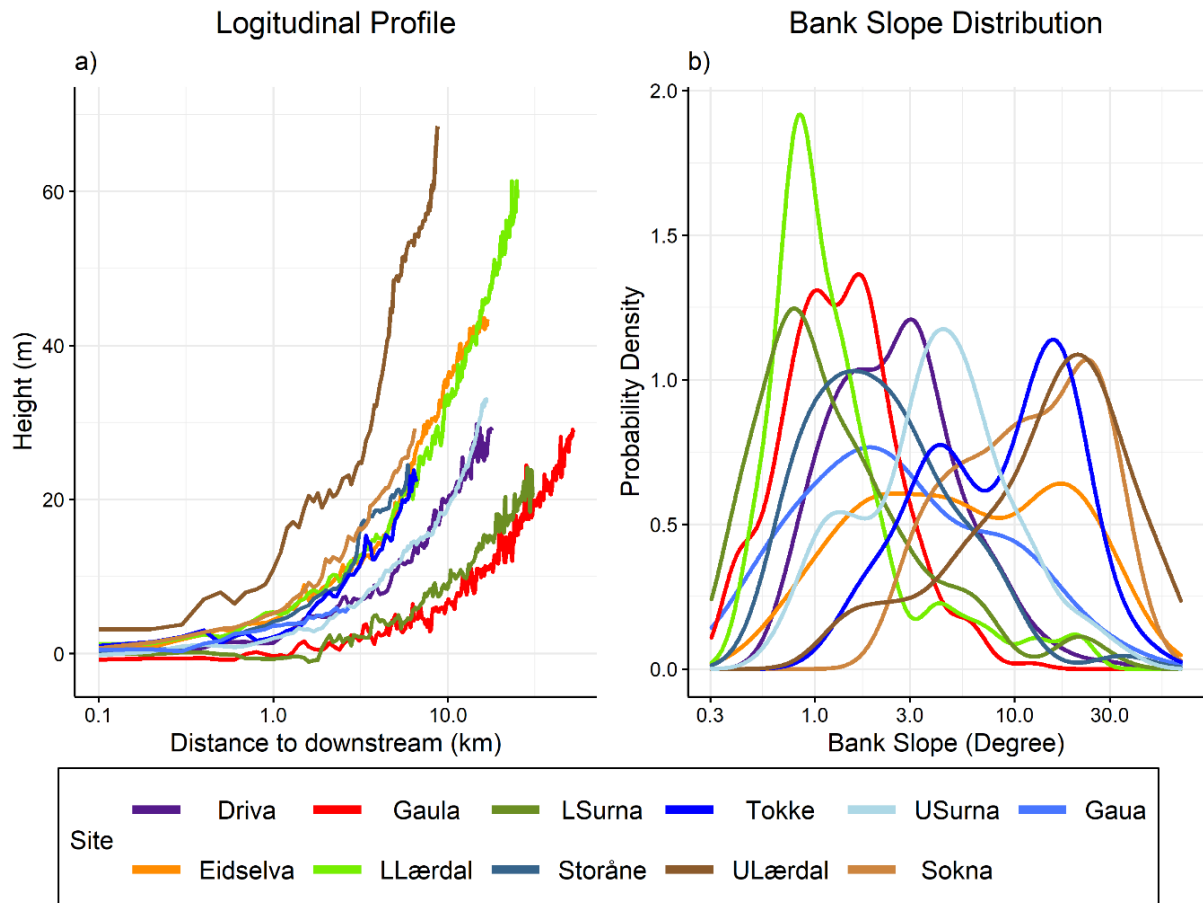
Figure 3. The longitudinal profile (**a**) and the bank slope distribution (**b**) for the 11 sites. U and L prior to Lærdal and Surna abbreviate Upper and Lower.

4.2. Inundation Error Development

Figure 4 shows an example of the obtained flood inundations from HEC-RAS for Gaula reach. It was noticeable that the inundation obtained by the *RL* model not only resulted in a larger inundation than the *GL*, but the overestimation also differed spatially. In some places, the two extents almost matched with minor differences, while in others, the variations were substantial.
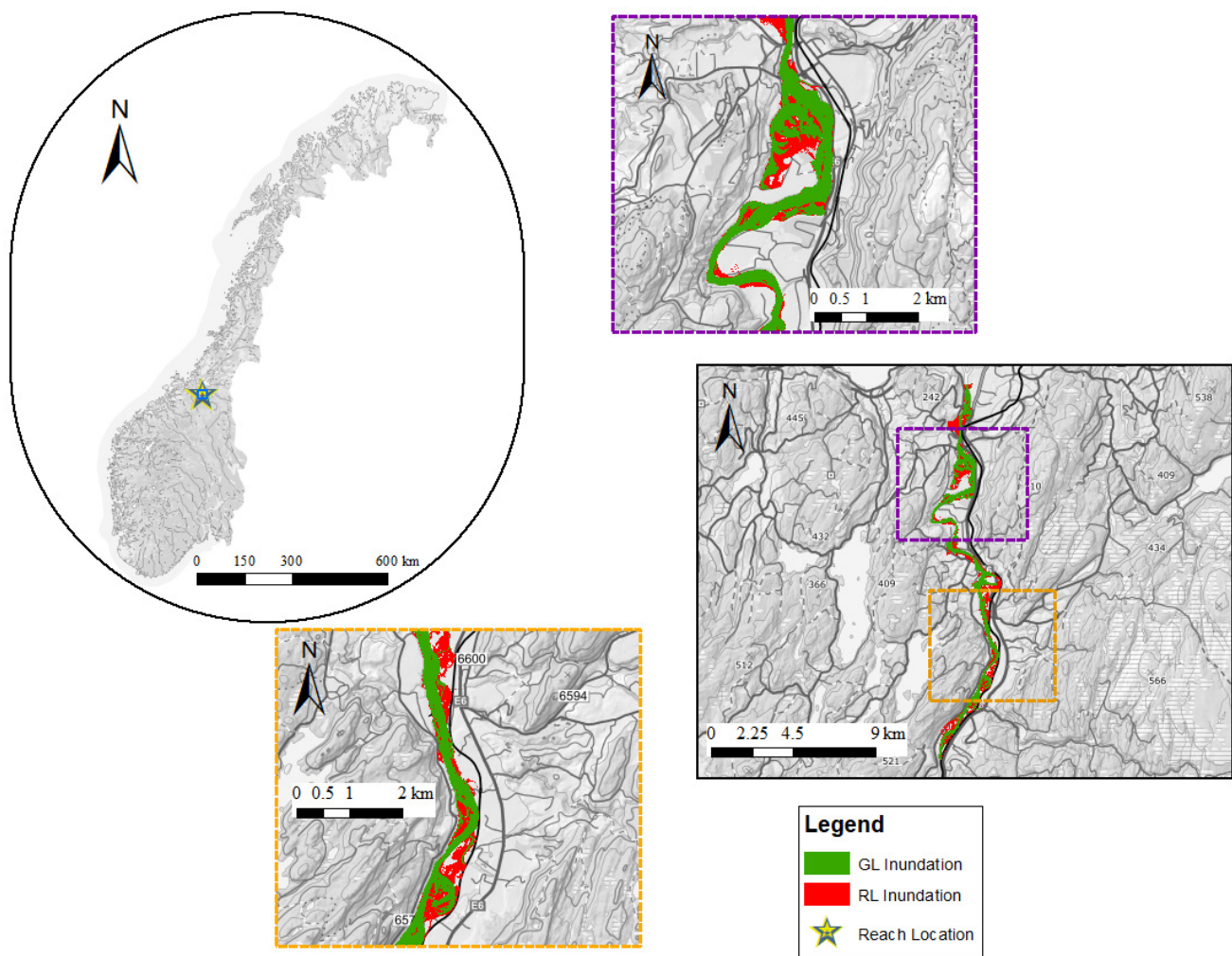
Figure 4. Flood extent for the 50-year return period scenario for the Gaula site using different LiDAR DEMs. *GL* and *RL* denote Green LiDAR and Red LiDAR, respectively.

Figure 5 shows the inundation errors for all the sites with respect to the flood's return period (T). The pattern of the error can be categorized into two types. The first was the continuous descending pattern in which the higher the flood size, the smaller was the Normalized Error, and that was seen in Gaua, Tokke, Storåne, and Upper Lærdal. The second category appears in Driva, Eidselva, Gaula, Upper Surna, Lower Surna, and Lower Lærdal, where the error peaks at a certain return period before it descends and follows the first trend. Lower Lærdal stands out as the reach with the highest error in general with two peaks.

The relationship between the error in inundation at a cross-sectional scale and the bank slope of the corresponding cross-section for different flood scenarios are shown in Figure 6. The sites Eidselva, Gaula, and Upper Lærdal covered the different ranges of the longitudinal slope and the bank slope among the tested sites, as shown in Figure 3a,b. In general, the cross-sections that have a lower mean bank slope's angle produced higher inundation errors. Meanwhile, the cross-sections that were associated with low standard deviation angles resulted in higher inundation's error too. Maintaining this relationship was found to diminish with the flood sizes increasing, and for Gaula sites, this relationship completely disappeared for the highest flood.
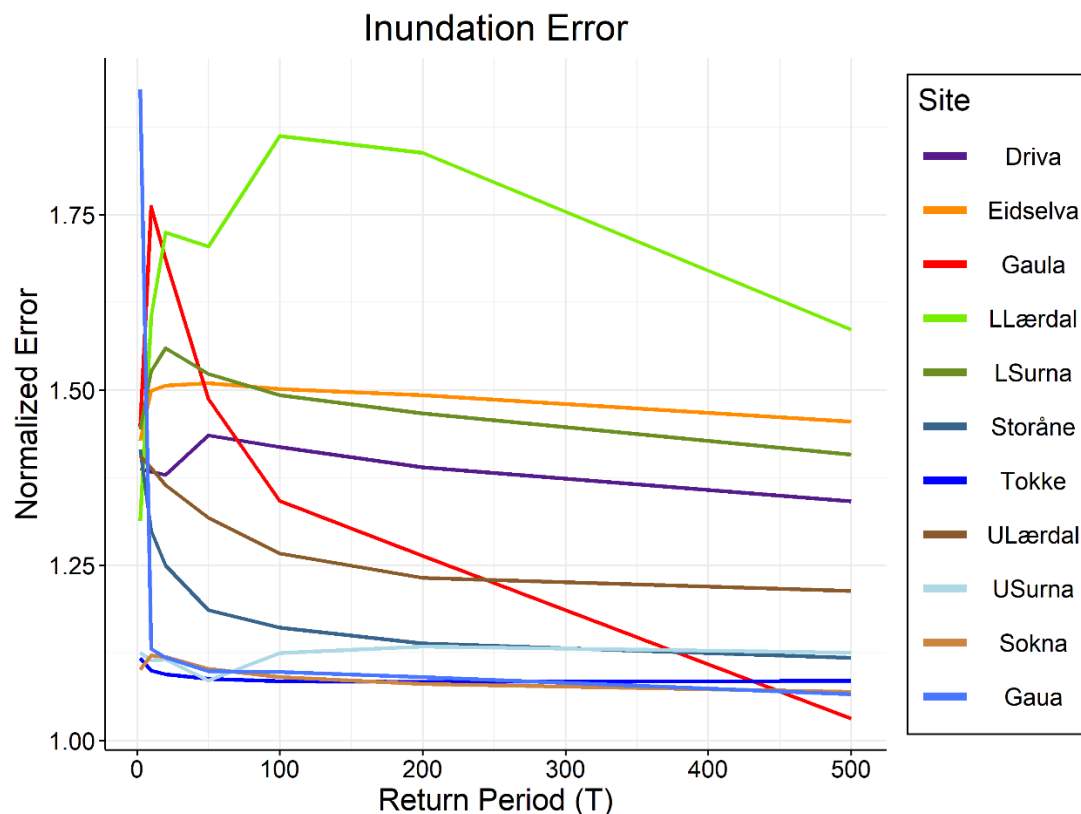
Figure 5. The inundation error comparison for the 11 sites. U and L prior to Lærdal and Surna abbreviate Upper and Lower.

4.3. Statistical Tests' Outputs

A statistical analysis ANOVA was conducted to predict the error shape by the flood protection coverage. The continuous decreasing trend was coded as 0 and the peaking trend as 1. The flood protection coverage was found to produce an F-statistic of 6.27 for a *p*-value less than 0.05. In addition, the analysis showed that for the sites that have flood protection coverage of 24% or more, they followed the peaking error trend.

For the error level investigation, a correlation test was carried out for the terrain parameters in Table 3 against the expectation of the inundation errors (the mean) of all the scenarios. The mean error was found to have positive correlations with the sinuosity ($r^2 = 0.72$) and the flood embankment coverage ($r^2 = 0.5$), and negative correlation with the mean bank slope ($r^2 = 0.44$).

4.4. Correction Techniques Outputs

The changes in the inundation errors that followed the application of the correction methods DCT and TCT on the Gaula and Lower Lærdal sites are shown in Figure 7. In general, both techniques resulted in reducing the error that stems from using the *RL* DEM. In all the scenarios, the reductions obtained by the TCT method were larger than using the DCT method, and for the 500-years scenario in Gaula, the reduction obtained by the TCT led to an underestimation of the *GL Inundation*, as can be seen in Figure 7a. The reduction in the error from the *RL* model for the two sites is presented in Figure 7c,d. The reductions obtained by the DCT and the TCT in the Gaula site were greater than in Lower Lærdal. The *Error Reduction* value for the 500-years flood scenario for Gaula is not shown due to the underestimation.
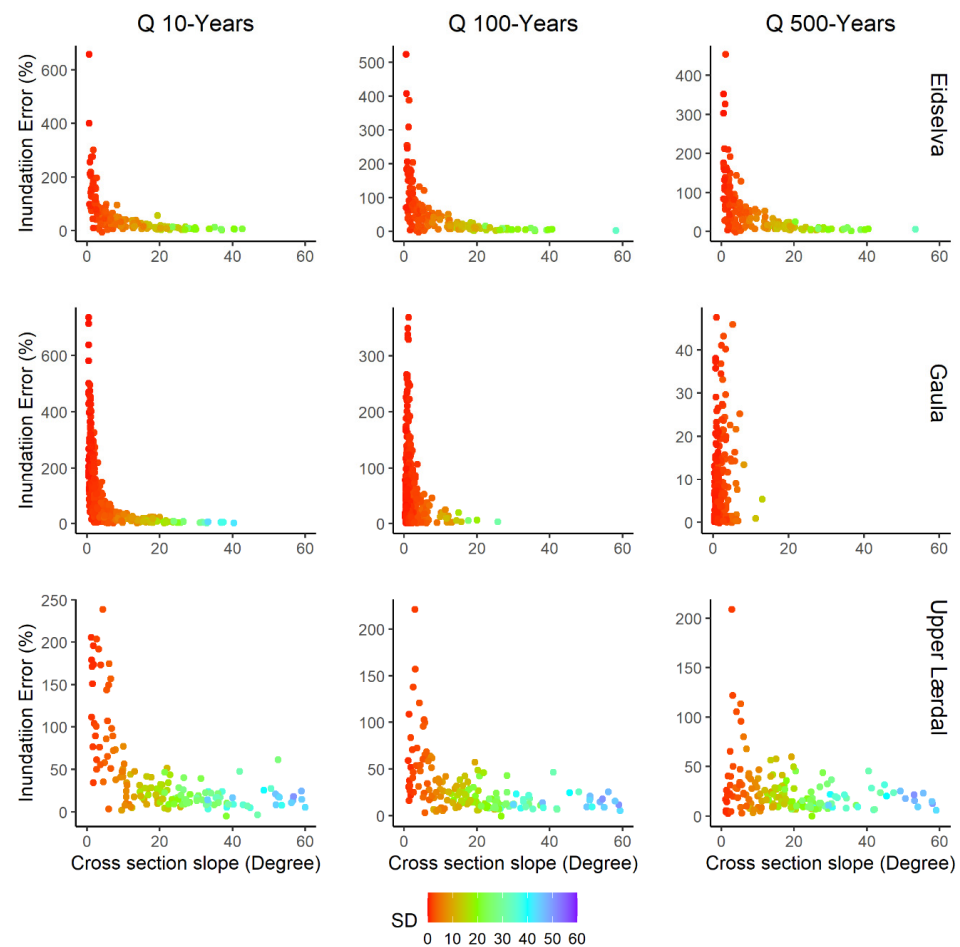
Figure 6. The relationship between the inundation error at the cross-section and the correspondence cross-section slope for Q-10-years, Q-100-years, and Q-500-years for Eidselva, Gaula, and Upper Lærdal. SD is the standard deviation of the bank slope at the cross-section in degrees.
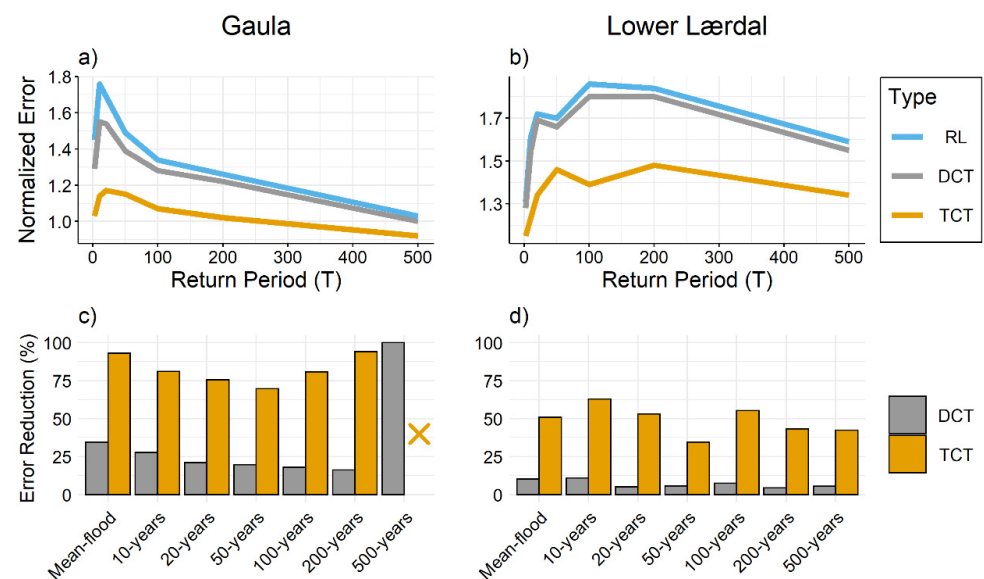
Figure 7. The inundation error for Gaula and Lower Lærdal sites after the terrain correction (TCT) and the discharge correction (DCT) techniques were applied (**a,b**) with the corresponding reduction in error for each scenario (**c,d**). The *Error Reduction* value in (**c**) for Gaula is omitted due to underestimation.

5. Discussion

5.1. Shape of the Inundation Error's Curve

An overestimation of the flood inundation for the sites was detected when the *RL* model was used compared to the *GL* model, and this can be seen in the example presented in Figure 4. Such an overestimation was also reported in previous studies that tested *RL* DEMs against referenced DEMs obtained by field measurements [21,22]. The magnitude of the overestimation varies with the flood scenario, as also seen in the study of Bures et al. [22]. Figure 5 shows that the inundation error's shape follows two trends, the continuous decreasing shape and the peaking shape. One of the links between the sites that have the peaking error shape is the amount of the flood embankment in the reach. The ANOVA analysis has shown that this parameter to be significant in predicting the peaking trend (F = 6.27, $p < 0.05$). In addition, the analysis showed that for the sites that have flood protection coverage of 24% or more, they follow the peaking error trend with Lower Lærdal and Gaula appearing as the most prominent sites, which confirms the results shown in Figure 5. This effect could be explained by Figure 8 as it illustrates an example of the embankment effect. Since the bottom of the river is elevated in the *RL* model, the flood walls will be overtopped in the *RL* model at a lower flood discharge than in the *GL* model and, therefore, creates larger deviation in inundation. As long as a larger flood scenario overtops the embankment in the *GL* model, the deviation will start to shrink and follow the normal decreasing trend. The study of Bradbrook et al. [39] also noted this deviation in such reaches.
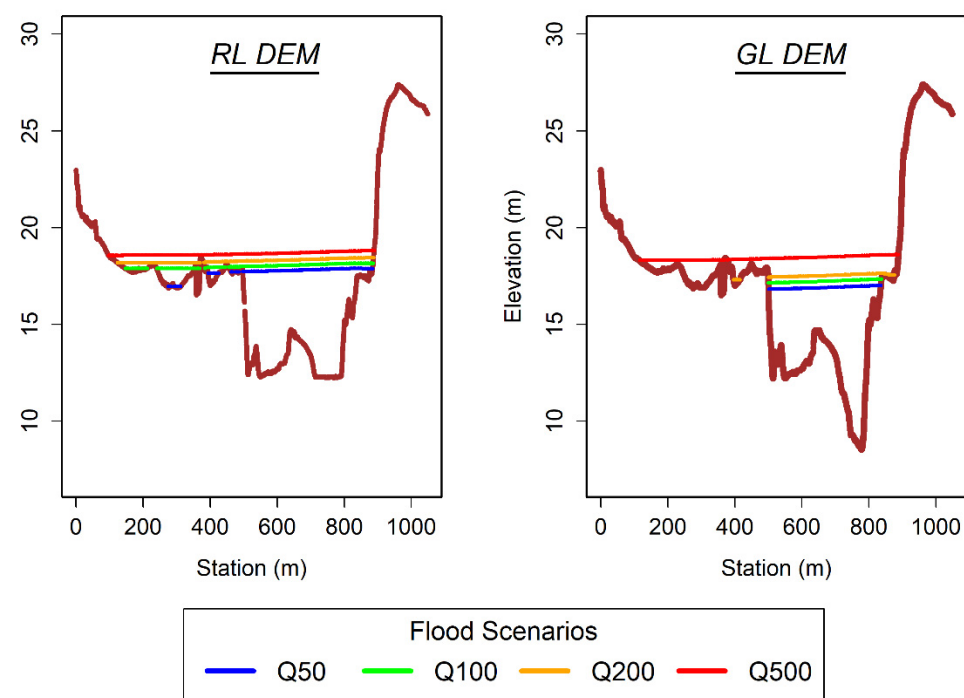
Figure 8. The water surface elevations for the flood levels Q50, Q100, Q200, and Q500 years for a cross-section in the Gaula site, using the different LiDAR DEMs.

5.2. Level of the Inundation Error

In addition to the error's shape, the level of the inundation error differs from one site to another, as shown in Figure 5. The overall level of the inundation error is different, for example, in Lower Lærdal than in Driva, even though they are both categorized as peaking error sites. The correlation test has shown that these levels have a tendency to increase where the sinuosity and the flood protection of the reach are higher, while increasing the bank slope angle, more steep cross-section, will decrease this level. However, this test is very rough to find a concrete conclusion on the error level as it hides the significance of

each parameter behind its unique value. For instance, the importance of the bank slope will diminish when the mean slope is only considered rather than the distribution or its standard deviation. Therefore, the bank slope is expected to have higher significance as it could be interpreted from Figure 6. Lower Lærdal appears to have the highest overall error levels among the other sites, and it is also featured with the highest percentage of flat cross-sections, as shown in Figure 3b. On the contrary, the sites that produce the least overall error levels, such as Sokna, Tokke, and Upper Lærdal, were associated with higher percentages of steep slopes than flat banks in their reach. However, some sites were not following the proposed trend. For instance, Storåne, even though it is among the sites with low error levels, has a high percentage of flat banks. However, the Storåne site is a steep reach and has zero coverage of flood protections, which could explain why it has a low error level.

5.3. Inundation's Error at Cross-Sectional Scales

The effect of the valley shape in various fluvial applications was investigated by many studies such as Rosgen [40], who investigated the relation of the valley shape to the channel formation and morphology, and Hassan and Reid [41], and Płaczkowska and Krzemień [42] who investigated the relation between river shape and sediment transport processes. Both of these studies show a relationship between river shape and fluvial processes, a relationship that we investigated for inundation error.

The total error that develops at the reach scale is an aggregation of the error's behavior at the cross-sectional level, and therefore, understanding the error at this level is equally important. As shown in Figure 6, the cross-sections with low mean bank slopes (flat cross-sections) are associated with high inundation errors, while cross-sections that have a low standard deviation in bank slope also produce high errors. This is in line with the fact that the flatter the bank's slope, the larger chance of higher inundation errors. The reason for that is because, for flat banks, a small overestimation of the flood level will inundate larger areas compared to a section with steep banks. Therefore, since the use of *RL* will create an overestimation of the flood levels, the errors in flat cross-sections will be more pronounced than the steep banks' rivers. Similarly, a bank slope with a low standard deviation implies a wide cross-section with considerable flat regions. In such cross-sections, the wider the cross-section, the lower the standard deviation, the higher is the inundation error. However, the dependency of the cross-sectional inundation error on the bank's slope diminishes with an increase in flood magnitude. This is shown in Figure 8 where the flood levels for both LiDAR models almost coincide, resulting in the same floodplain inundation.

5.4. Flood Model Correction

Generally, the correction methods have shown improvements on the *RL* inundations as they reduced the error to some extent. However, the TCT has shown to be more efficient in reducing the error in inundations since the reduction of the RL's overestimation was higher than what was obtained by the DCT, as can be seen in Figure 7. A similar finding was reported by Choné et al. [23], where the flood levels were obtained for two sites using these correction methods. One of the conclusions was that the DCT is associated with an underestimation of the flow velocity resulting from the assumption that the flow is divided into two components, and that will eventually result in an overestimation of the flood levels. However, both correction methods worked better in Gaula than in Lower Lærdal. The ratio of the LiDAR discharge to the mean discharge of Gaula is approximately four times larger than Lower Lærdal, and that, to a large extent, explains why reducing the LiDAR discharge from the flood discharge in Gaula is more efficient than in Lower Lærdal. Similarly, the amount of the missed LiDAR volume in Gaula was found to be much larger than in Lower Lærdal, as shown in Table 3 (141 and 8 m^3/m, respectively). The fact that the TCT method worked better in Gaula is well explained by this finding since the TCT is based on carving out this excess subsurface volume occupied by the LiDAR discharge. It should also be noted that in the case of small inundation errors, applying the correction

methods might result in an underestimation of the inundation as is encountered in the 500-years scenario in Gaula shown in Figure 7a,c which was also was found in the study of Choné et al. [23].

6. Conclusions

A comparison was conducted between the *RL* and *GL* terrain models in producing flood inundation extent for 11 sites in Norway. The use of the *RL* to produce flood inundation is associated with deviations from the actual inundation, and this deviation follows two trends: a continuously decreasing deviation in inundation with the flood size increase and an increasing pattern of the deviation with the flood size increase to a certain peak before it starts to decrease again. These trends were found to be associated with flood embankment coverage of the reach of which the ones with less than 25% coverage follow the first trend. In addition, the level of the inundation error was found to positively correlate with the sinuosity and the embankment coverage and negatively with the bank slope angle of the reach. Possible corrections for the *RL* inundations could be achieved by using the TCT and the DCT, of which the former resulted in better improvements. However, both corrections were found to work better in sites where the accompanying effects of the LiDAR's acquisition have more impact on the *RL* data, while in sites where the error is more attributed to the reach's configuration, the corrections were less efficient. Therefore, the use of the pure *RL* DEMs for flood map generation should be handled with caution and particularly for small flood sizes and, even more caution, in reaches with a large number of embankments, as this could lead to high inundation errors even at high flood scenarios.

Author Contributions: Conceptualization, K.A., M.O.M.A. and A.J.; methodology, M.A, K.A. and A.J.; validation, M.O.M.A.; formal analysis, M.O.M.A.; investigation, M.O.M.A.; resources, K.A.; data curation, M.O.M.A.; writing—original draft preparation, M.O.M.A.; writing—review and editing, M.O.M.A. and K.A.; visualization, M.O.M.A., K.A. and A.J.; supervision, K.A. and A.J.; project administration, K.A.; funding acquisition, K.A. All authors have read and agreed to the published version of the manuscript.

Funding: Mahmoud Awadallah was partly funded by the project "Evaluation of green LiDAR", funded by The Norwegian Water Resources and Energy Directorate (NVE). Ana Juárez was funded by the Norwegian Research Council project TryggElv (project number: 309731).

Institutional Review Board Statement: Not applicable.

Informed Consent Statement: Not applicable.

Data Availability Statement: Data available upon request to Mahmoud Omer Mahmoud Awadallah.

Acknowledgments: The authors wish to thank the four reviewers for their thorough and constructive comments. The authors also wish to thank The Norwegian Mapping Authority, NVE, Statkraft, and Eco-Hafslund for providing access to the LiDAR data.

Conflicts of Interest: The authors declare no conflict of interest.

Appendix A

Flow diagram of the main steps of the methodology.
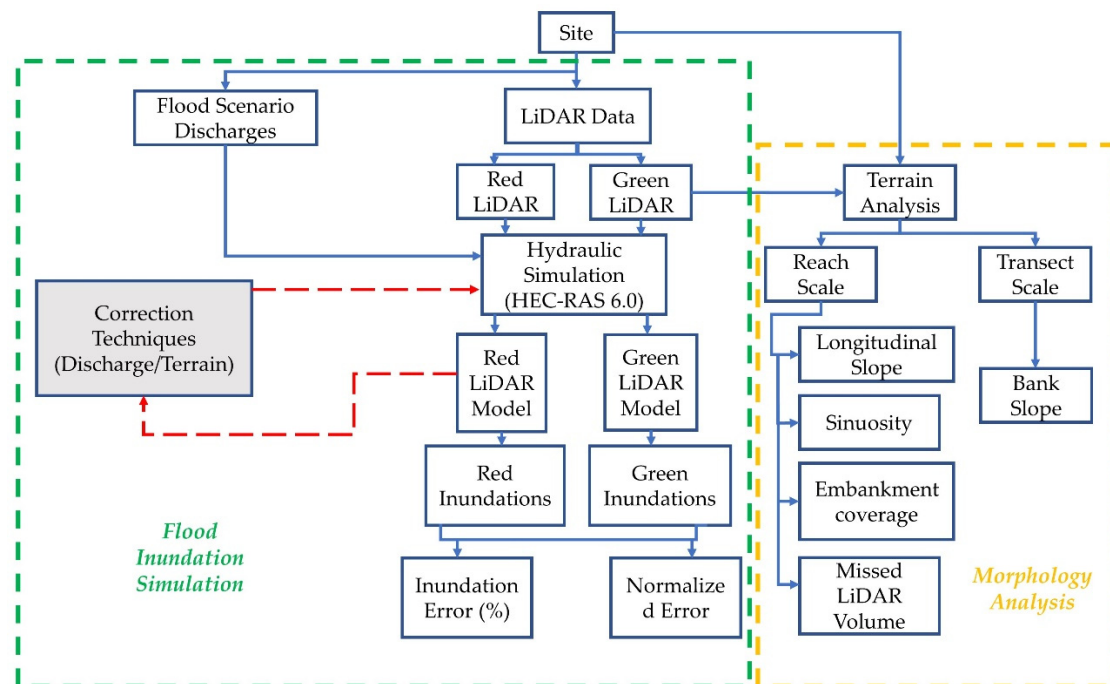
Figure A1. Flow diagram of the main steps of the methodology.

References

1. Ciscar, J.C.; Iglesias, A.; Feyen, L.; Szabó, L.; Van Regemorter, D.; Amelung, B.; Nicholls, R.; Watkiss, P.; Christensen, O.B.; Dankers, R.; et al. Physical and economic consequences of climate change in Europe. *Proc. Natl. Acad. Sci. USA* **2011**, *108*, 2678–2683. [CrossRef] [PubMed]
2. Christensen, J.H.; Christensen, O.B. Severe summertime flooding in Europe. *Nature* **2003**, *421*, 805–806. [CrossRef] [PubMed]
3. Frei, C.; Schöll, R.; Fukutome, S.; Schmidli, J.; Vidale, P.L. Future change of precipitation extremes in Europe: Intercomparison of scenarios from regional climate models. *J. Geophys. Res. Atmos.* **2006**, *111*. [CrossRef]
4. Blöschl, G.; Hall, J.; Parajka, J.; Perdigão, R.A.P.; Merz, B.; Arheimer, B.; Aronica, G.T.; Bilibashi, A.; Bonacci, O.; Borga, M.; et al. Changing climate shift timing of European floods. *Science* **2017**, *357*, 588–590. [CrossRef] [PubMed]
5. Lawrence, D. Uncertainty introduced by flood frequency analysis in projections for changes in flood magnitudes under a future climate in Norway. *J. Hydrol. Reg. Stud.* **2020**, *28*, 100675. [CrossRef]
6. Rözer, V.; Müller, M.; Bubeck, P.; Kienzler, S.; Thieken, A.; Pech, I.; Schröter, K.; Buchholz, O.; Kreibich, H. Coping with pluvial floods by private households. *Water* **2016**, *8*, 304. [CrossRef]
7. Tanaka, T.; Kiyohara, K.; Tachikawa, Y. Comparison of fluvial and pluvial flood risk curves in urban cities derived from a large ensemble climate simulation dataset: A case study in Nagoya, Japan. *J. Hydrol.* **2020**, *584*, 124706. [CrossRef]
8. Apel, H.; Martínez Trepat, O.; Nghia Hung, N.; Thi Chinh, D.; Merz, B.; Viet Dung, N. Combined fluvial and pluvial urban flood hazard analysis: Concept development and application to Can Tho city, Mekong Delta, Vietnam. *Nat. Hazards Earth Syst. Sci.* **2016**, *16*, 941–961. [CrossRef]
9. Zurich Insurance Group. *Three Common Types of Flood Explained*; Zurich Insurance Group: Zurich, Switzerland, 2020. Available online: https://www.zurich.com/en/knowledge/topics/flood-and-water-damage/three-common-types-of-flood (accessed on 16 May 2021).
10. U.S. Geological Survey. *US GeoData Digital Elevation Models*; U.S. Geological Survey: Reston, VA, USA, 2000; Fact Sheet.
11. Muhadi, N.A.; Abdullah, A.F.; Bejo, S.K.; Mahadi, M.R.; Mijic, A. The use of LiDAR-derived DEM in flood applications: A review. *Remote Sens.* **2020**, *12*, 2308. [CrossRef]
12. Jarihani, A.A.; Callow, J.N.; McVicar, T.R.; Van Niel, T.G.; Larsen, J.R. Satellite-derived Digital Elevation Model (DEM) selection, preparation and correction for hydrodynamic modelling in large, low-gradient and data-sparse catchments. *J. Hydrol.* **2015**, *524*, 489–506. [CrossRef]
13. Hafezi, M.; Sahin, O.; Stewart, R.A.; Mackey, B. Creating a novel multi-layered integrative climate change adaptation planning approach using a systematic literature review. *Sustainability* **2018**, *10*, 4100. [CrossRef]
14. Wang, Y.; Chen, A.S.; Fu, G.; Djordjević, S.; Zhang, C.; Savić, D.A. An integrated framework for high-resolution urban flood modelling considering multiple information sources and urban features. *Environ. Model. Softw.* **2018**, *107*, 85–95. [CrossRef]

15. Lefsky, M.A.; Cohen, W.B.; Parker, G.G.; Harding, D.J. Lidar remote sensing for ecosystem studies. *Bioscience* **2002**, *52*, 19–30. [CrossRef]

16. Dowman, I. Integration of LIDAR and IFSAR for mapping. *Int. Arch. Photogramm. Remote Sens.* **2004**, *35*, 90–100.

17. Hodgson, M.E.; Jensen, J.R.; Schmidt, L.; Schill, S.; Davis, B. An evaluation of LIDAR- and IFSAR-derived digital elevation models in leaf-on conditions with USGS Level 1 and Level 2 DEMs. *Remote Sens. Environ.* **2003**, *84*, 295–308. [CrossRef]

18. Bhuyian, M.N.M.; Kalyanapu, A. Accounting digital elevation uncertainty for flood consequence assessment. *J. Flood Risk Manag.* **2018**, *11*, S1051–S1062. [CrossRef]

19. McClean, F.; Dawson, R.; Kilsby, C. Implications of Using Global Digital Elevation Models for Flood Risk Analysis in Cities. *Water Resour. Res.* **2020**, *56*, e2020WR028241. [CrossRef]

20. Muthusamy, M.; Casado, M.R.; Butler, D.; Leinster, P. Understanding the effects of Digital Elevation Model resolution in urban fluvial flood modelling. *J. Hydrol.* **2021**, *596*, 126088. [CrossRef]

21. Casas, A.; Benito, G.; Thorndycraft, V.R.; Rico, M. The topographic data source of digital terrain models as a key element in the accuracy of hydraulic flood modelling. *Earth Surf. Processes Landf.* **2006**, *31*, 444–456. [CrossRef]

22. Bures, L.; Roub, R.; Sychova, P.; Gdulova, K.; Doubalova, J. Comparison of bathymetric data sources used in hydraulic modelling of floods. *J. Flood Risk Manag.* **2019**, *12*, e12495. [CrossRef]

23. Choné, G.; Biron, P.M.; Buffin-Bélanger, T. Flood hazard mapping techniques with LiDAR in the absence of river bathymetry data. *E3S Web Conf.* **2018**, *40*, 06005. [CrossRef]

24. Dey, S.; Saksena, S.; Merwade, V. Assessing the effect of different bathymetric models on hydraulic simulation of rivers in data sparse regions. *J. Hydrol.* **2019**, *575*, 838–851. [CrossRef]

25. Reil, A.; Skoulikaris, C.; Alexandridis, T.K.; Roub, R. Evaluation of riverbed representation methods for one-dimensional flood hydraulics model. *J. Flood Risk Manag.* **2018**, *11*, 169–179. [CrossRef]

26. Hilldale, R.C.; Raff, D. Assessing the ability of airborne LiDAR to map river bathymetry. *Earth Surf. Processes Landf.* **2008**, *33*, 773–783. [CrossRef]

27. Irish, J.L.; Lillycrop, W.J. Scanning laser mapping of the coastal zone: The SHOALS system. *ISPRS J. Photogramm. Remote Sens.* **1999**, *54*, 123–129. [CrossRef]

28. Kinzel, P.J.; Legleiter, C.J.; Nelson, J.M. Mapping River Bathymetry With a Small Footprint Green LiDAR: Applications and Challenges. *J. Am. Water Resour. Assoc.* **2013**, *49*, 183–204. [CrossRef]

29. Mandlburger, G.; Hauer, C.; Wieser, M.; Pfeifer, N. Topo-Bathymetric LiDAR for Monitoring River Morphodynamics and Instream Habitats-A Case Study at the Pielach River. *Remote Sens.* **2015**, *7*, 6160–6195. [CrossRef]

30. Breili, K.; Simpson, M.J.R.; Klokkervold, E.; Roaldsdotter Ravndal, O. High accuracy coastal flood mapping for Norway using LiDAR data. *Nat. Hazards Earth Syst. Sci. Discuss.* **2019**, *20*, 673–694. [CrossRef]

31. Gottschalk, L.; Jensen, L.J.; Lundquist, D.; Solantie, R.; Tollan, A. Hydrologic regions in the Nordic countries. *Nord. Hydrol.* **1979**, *10*, 273–286. [CrossRef]

32. Engeland, K.; Glad, P.; Hamududu, B.H.; Li, H.; Reitan, T.; Stenius, S. *Lokal og Regional Flomfrekvensanalyse*; Rapport nr. 10/2020; Norges Vassdrags-og Energidirektorat: Oslo, Norway, 2020; ISBN 9788241020148. Available online: https://publikasjoner.nve.no/rapport/2020/rapport2020_10.pdf (accessed on 3 January 2022).

33. Brunner. *Hydraulic Reference Manual*; US Army Corps of Engineers: Washington, DC, USA, 1995; pp. 1–2.

34. Cook, A.; Merwade, V. Effect of topographic data, geometric configuration and modeling approach on flood inundation mapping. *J. Hydrol.* **2009**, *377*, 131–142. [CrossRef]

35. Jung, H.C.; Jasinski, M.; Kim, J.W.; Shum, C.K.; Bates, P.; Neal, J.; Lee, H.; Alsdorf, D. Calibration of two-dimensional floodplain modeling in the central Atchafalaya Basin Floodway System using SAR interferometry. *Water Resour. Res.* **2012**, *48*, 1–13. [CrossRef]

36. Chow, V.T. *Open Channel Hydraulics*; McGraw-Hill: New York, NY, USA, 1959.

37. Wei, T.; Simko, V. R Package "Corrplot": Visualization of a Correlation Matrix. 2021. Available online: https://github.com/taiyun/corrplot (accessed on 10 May 2021).

38. Fox, J.; Weisberg, S. *An {R} Companion to Applied Regression*, 3rd ed.; Sage: Thousand Oaks, CA, USA, 2019.

39. Bradbrook, K.F.; Lane, S.N.; Waller, S.G.; Bates, P.D. Two dimensional diffusion wave modelling of flood inundation using a simplified channel representation. *Int. J. River Basin Manag.* **2004**, *2*, 211–223. [CrossRef]

40. Rosgen, D.L. A classification of natural rivers. *Catena* **1994**, *22*, 169–199. [CrossRef]

41. Hassan, M.A.; Reid, I. The influence of microform bed roughness elements on flow and sediment transport in gravel bed rivers. *Earth Surf. Process. Landf.* **1990**, *15*, 739–750. [CrossRef]

42. Płaczkowska, E.; Krzemień, K. Natural conditions of coarse bedload transport in headwater catchments (Western Tatras, Poland). *Geogr. Ann. Ser. A Phys. Geogr.* **2018**, *100*, 370–387. [CrossRef]